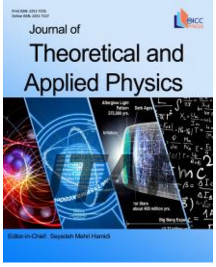

J. Theor. Appl. Phys 2026; 20(1): 69-81

Journal of Theoretical and Applied Physics
(JTAP)

https://doi.org/10.57647/jtap.2026.2001.07

Research Article

Physical Properties of Common Two-Temperature Fusion Plasmas

Mehdi Kavehnia[1], Hossein Sadeghi[1], Seyede Nasrin Hosseinimotlagh[2*]

[1]*Department of Physics, Faculty of Sciences, Arak University, Arak, 38156-8-8349, Iran*
[2]*Department of Physics, Shi., C., Islamic Azad University, Shiraz, Iran*

***Corresponding author:** nasrinhosseini _ motlagh@iau.ir

Article History:

Received:
31 May 2025

Revised:
09 September 2025

Accepted:
04 October 2025

Published Online:
16 December 2025

Published in Issue:
28 February 2026

Abstract

Here, we investigate thermal relaxation dynamics in dense, non-isothermal plasmas using a binary plasma framework combined with the effective interaction potential method, which is crucial for understanding thermonuclear burn processes. The analysis covers primary fusion fuels, including DT (neutron-yielding) and aneutronic fuels such as D^3He and $p^{11}B$. Electron and ion temperatures (T_e and T_i) are considered independently, since intra-species equilibration occurs significantly faster than inter-species energy exchange due to the substantial mass difference. Addressing the computational challenges associated with simulating confined fusion plasmas arising from multiple coupled physical phenomena we introduce, for the first time, the effective interaction potential approach as a computationally efficient and accurate method for dense plasma systems. These potentials account for both (i) long-range charge overlap effects and (ii) short-range quantum interactions. Within this framework, we evaluate critical plasma properties, including stopping power, deceleration time, energy transfer coefficients, absorbed energy, and temperature relaxation rates for $p^{11}B$, D^3He, and DT fuels, providing valuable insights into the optimal conditions for thermonuclear performance.

Keywords: Dense plasma, fuel, Hot, Temperature relaxation, Effective interaction potential

Cite this article: Kavehnia, M., Sadeghi, H., Hosseinimotlagh,S.N., (2026). Physical Properties of Common Two-Temperature Fusion Plasmas. *J. Theor. Appl. Phys*., 20(1), 69-81. https://doi.org/10.57647/jtap.2026.2001.07

1. Introduction

Hydrogen plasmas with high-temperature, such as those produced in ICF experiments or naturally occurring in stellar cores, constitute the primary medium for thermonuclear fusion reactions. Within these plasmas, ions undergo fusion reactions, generating energetic alpha particles that subsequently transfer energy to both electrons and ions via Coulomb collisions. Owing to the substantial mass difference between electrons and ions, this energy transfer is initially uneven, leading to separate electron (T_e) and ion (T_i) temperature distributions. Therefore, a detailed understanding of electron–ion temperature relaxation dynamics is essential for accurately predicting ignition thresholds and enhancing fusion efficiency [1–4]. ICF experiments, precise knowledge of the hot spot temperature is of paramount importance. Ion temperatures can be inferred from the spectral broadening of fusion reaction products [5–7], whereas electron temperatures are primarily determined from the radiation emitted by free electrons scattering off ions. Due to their lower mass and higher mobility, electrons predominantly shape the observed emission spectrum, making T_e a crucial diagnostic quantity [8 , 9].

Dense plasmas produced in laboratory settings or encountered in astrophysical environments frequently exist in a state far from thermal equilibrium. For instance, ultra-cold neutral plasmas and high-density laser-generated plasmas can exhibit electron and ion temperatures that differ by an order of magnitude or more [1–5]. Accurate modeling of such non-equilibrium systems necessitates extending conventional ideal-gas kinetic theory to account for strong interparticle correlations, collective screening effects, and quantum mechanical corrections [10–12].

In the present study, we utilize the effective interaction potential approach to examine temperature relaxation and energy transfer characteristics in non-isothermal dense plasmas. This method enables accurate and computationally efficient modeling of electron ion interactions in systems where multiple physical effects such as quantum degeneracy, screening, and strong coupling are prominent [13–15].

Specifically, the approach incorporates:

i. Long-range collective effects, arising from charge screening in dense plasma environments.

ii. Short-range quantum effects, which become important at interparticle distances comparable to the de Broglie wavelength. The effective interaction potential, $\Phi_{\alpha\beta}(r)$, is defined as:

$$\Phi_{\alpha\beta}(r) = \frac{1}{2\pi^2} \int \Phi_{\alpha\beta}(r) \exp(ik \cdot r)/\epsilon(k,\omega)\ d^3k \qquad (1)$$

Here, $\Phi_{\alpha\beta}(r)$ represents the pairwise interaction potential, and $\varepsilon(k,\omega)$ denotes the plasma dielectric function. A commonly employed approximation for point-charge screening is the Yukawa's potential:

$$\Phi_Y(r, T, n) = Q_1 \times Q_2 \frac{\exp\left(-k_Y r\right)}{r} \qquad (2)$$

Here, k_Y is the inverse Debye (Yukawa) screening length, which can be obtained either from the Fermi model or from the long-wavelength limit of the polarization function within RPA (random phase approximation) [15–18] .By employing these effective interaction potentials, key plasma properties such as stopping power, energy transfer rates, temperature relaxation times, and correlation energies of electrons and ions can be accurately calculated. This framework offers a reliable approach for investigating non-isothermal plasmas relevant to $p^{11}B$, D^3He, and DT fusion fuels, where precise modeling of electron ion energy exchange is critical for predicting ignition conditions and optimizing fusion reactor performance. The present study addresses a crucial gap in plasma simulating by integrating quantum corrections and effects of collective screening within a computationally efficient framework.

2. Plasma waves

Plasmas support a wide range of wave modes in both laboratory and space environments, each characterized by distinct linear and nonlinear behaviors. Among these, dust-acoustic waves, ion-acoustic waves, and electron-acoustic waves (EAWs) have been the focus of extensive research in recent years [6–10, 19]. These wave modes frequently exhibit rich nonlinear phenomena, including harmonic generation, instabilities, solitary structures, and shock formation. Electron-acoustic waves (EAWs) emerge in plasma systems containing two distinct electron populations, commonly referred to as hot and cold electrons, distinguished by their respective energy distributions. In this configuration, hot electrons, possessing high thermal velocities, provide the restoring force with minimal viscous resistance, while the slower-moving cold electrons contribute the system's inertia [20–23]. The phase velocity of EAWs falls between the thermal speeds of the cold and hot electrons, being considerably lower than that of the hot electrons but substantially higher than that of the cold electrons [24–26]. Due to their relatively large mass, ions are typically treated as a uniform neutralizing background. Electron-acoustic modes exhibit frequencies exceeding those of ion-acoustic waves, highlighting their significance in both laboratory and space plasma environments [27 , 28].

Interest in electron-acoustic waves (EAWs) has increased due to their experimental observation in controlled laboratory plasmas and their natural occurrence in space. Strongly excited EAWs can sustain nonlinear coherent structures, including solitons, shocks, and double layers [29].

In a typical two-temperature electron plasma, cold electrons provide the system's inertia, hot electrons act as the restoring force, and ions serve as a stationary background. These waves are particularly relevant for investigations of intense dense plasmas, warm dense matter, and plasmonic applications [30]. Shock waves in plasmas, a type of nonlinear phenomenon, are characterized by abrupt variations in pressure, temperature, and density. Their formation arises from a delicate interplay between nonlinearity and dissipation, and they have been studied both theoretically and experimentally in laser-produced plasmas and pure electron plasmas [29 , 30]. A thorough understanding of electron-acoustic wave dynamics and the associated shock structures is essential for applications spanning space physics, inertial confinement fusion, and high-energy-density plasma research.

3. Effective interaction potential of electron-ion

The effective electron–ion interaction potential is a key parameter for characterizing the properties of dense, non-isothermal plasmas. Within the framework of the random phase approximation (RPA), the dielectric function is formulated as [31].

The electron-ion effective interaction potential is a fundamental parameter in describing the behavior of dense, non-isothermal plasmas. Within the random phase approximation (RPA), the dielectric function is expressed as [31]:

$$\epsilon(k;0) = \frac{-4\pi e^2}{k^2}\left(\Pi_{RPA}(k) + Z^2\Pi_{ion}(k)\right) + 1 \qquad (3)$$

Here, $\Pi_{ion}(k)$denotes the ion polarization function, which, in the classical limit, can be approximated as $\Pi_{ion}(k) = -n_i/(k_B T_i)$. Figure 1 illustrates $\Pi_{ion}(k)$ variations with ion temperature T_i for the three fusion fuels: p^{11}B, D^{3}He, and DT. As observed, $\Pi_{ion}(k)$ decreases nonlinearly with increasing T_i. Among the fuels considered, DT exhibits the highest polarization, whereas the aneutronic fuels D^{3}He and p^{11}B display nearly identical, lower values.

The electron contribution, $\Pi_{RPA}(k)$, corresponds to the quantum polarization function at limit temperature is expressed as:

$$\Pi_{RPA}(\omega;k) = \frac{k^2\chi_0^2}{16\pi e^2 Z^3}\left[g_3(u-\mathcal{Z}) - g_3(u+\mathcal{Z})\right] \qquad (4)$$

Here, $\omega_P^2 = 4\pi m_e^{-1} n_e e^2$, $k_F{}^3 = 3\pi^2 n_e$, $\chi_0 = \sqrt{3/16}\,\hbar\omega_P/E_F$, $\mathcal{Z} = 0.5\frac{k}{k_F}$, $u = \frac{\omega}{k.v_F}$, and v_F denotes the Fermi velocity. Figures 2 and 3 illustrate the temperature dependence of u and Z for the three fusion fuels. The results show that u decreases nonlinearly with increasing temperature, while Z exhibits a nonlinear increase. Among the fuels, DT displays the highest u values, whereas P^{11}B reaches the largest Z values.

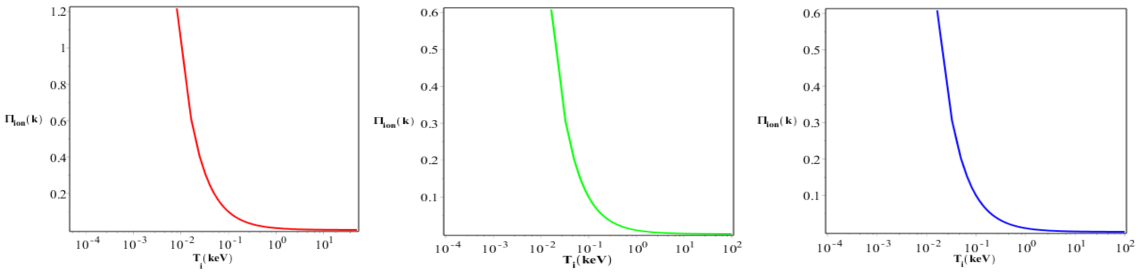

(a) (b) (c)

Figure 1. Variations of the ion polarization function, $\Pi_{ion}(k)$, versus ion temperature $T_i$for reactions: a: DT, b: P^{11}B, and c: D^{3}He

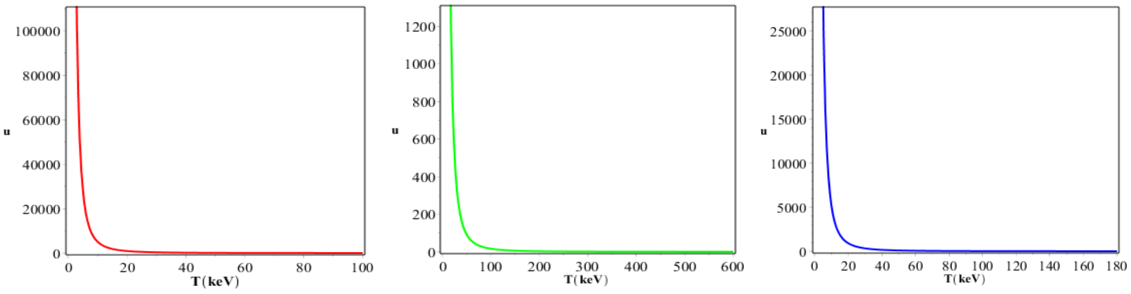

(a) (b) (c)

Figure 2. Temperature dependence of u for reactions: a: DT, b: P^{11}B, and c: D^{3}He

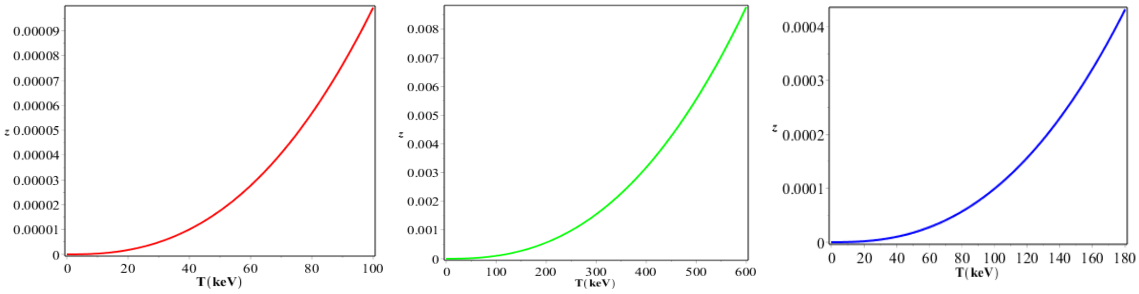

(a) (b) (c)

Figure 3. Temperature dependence of Z for reactions: a: DT, b: P^{11}B, and c: D^{3}He

10.57647/jtap.2026.2001.07

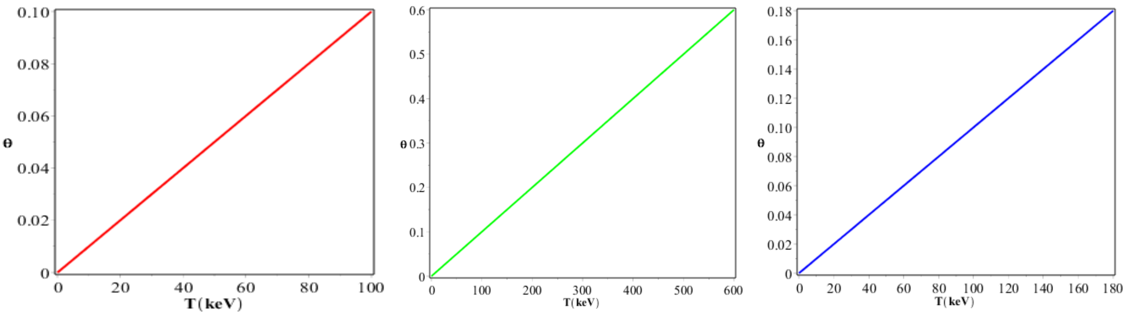

(a) (b) (c)

Figure 4. Temperature dependence of θ for reactions: a: DT, b: $P^{11}B$, and c: D^3He

The function $g_3(x)$ is defined as:

$$g_3(x) = -g_3(-x) = \int \frac{y\,dy}{\exp(y^2/\theta - \eta) + 1} \ln\left|\frac{x+y}{x-y}\right| \tag{5}$$

Here, $\theta = k_B T/E_F$ represents the degeneracy parameter, and $\eta = \mu/k_B T$denotes the normalized chemical potential. Figure 4 shows the θ variations with temperature for the three fusion fuels DT, $P^{11}B$, and D^3He. The results indicate a monotonically increasing trend, with D^3He exhibiting the highest values among the fuels considered.

The effective electron-ion potential is then expressed as [32]:

$$\Phi_{ei}(r) = e^2 Z \frac{\left[1 - e^{-r/\lambda_{ei}}\right]}{r} \tag{6}$$

Here, $\lambda_{ei} = \hbar/(\pi m_{ei} k_B T_{ei})^{1/2}$ is the thermal de Broglie wavelength characterizing quantum effects, m_{ei} = reduced mass of the electron-ion pair, and Z = ion charge number [33]. Figure 5 compares the 3D variations of λ_{ei} with Ti and Te for the three fuels. As observed, λ_{ei}increases with decreasing Ti but decreases with increasing Te Among the fuels, the hierarchy is $\lambda_{ei,D3He} > \lambda_{ei,DT} > \lambda_{ei,p11B}$.

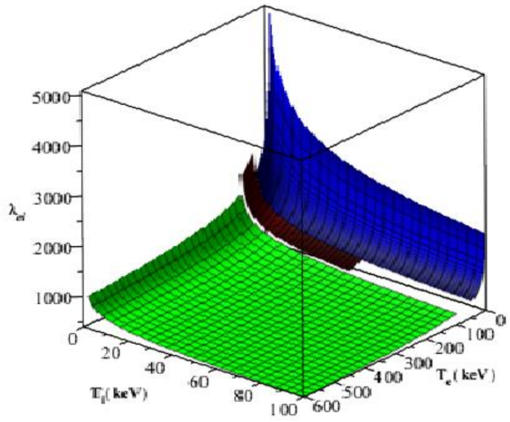

Figure 5. 3D comparison of $\boldsymbol{\lambda_{ei}}$ versus ion temperature T_i and electron temperature T_e for reactions: DT (red), D^3He (blue), and $p^{11}B$ (green)

For non-isothermal plasmas, the effective electron-ion temperature T_{ei} is introduced to capture the combined electron-ion interactions [34]:

$$T_{ei} = \sqrt{T_e T_i} \tag{7}$$

The full effective potential including quantum and screening effects is then represented as [35]:

$$\Phi_{ei} = \frac{Ze^2}{r\lambda_{ee}^2\gamma^2\sqrt{1-(2\,k_D/\lambda_{ee}\gamma^2)^2}}$$

$$\left[\left(\frac{1-\lambda_{ee}^2 B^2}{1-\lambda_{ei}^2 B^2}\right)\exp(-rB) - \left(\frac{1-\lambda_{ee}^2 A^2}{1-\lambda_{ei}^2 A^2}\right)\exp(-rA)\right] \tag{8}$$

$$+\frac{Ze^2\exp(-r/\lambda_{ei})}{r(1+C_{ei})}$$

Here the parameters A , B, C_{ei}, γ, λ_{ee} and k_i are defined by Eqs. 9 to 14.

$$A = (\gamma^2/2\left[1+\sqrt{1-(2\,k_D/\lambda_{ee}\gamma^2)^2}\right])^{\frac{1}{2}} \tag{9}$$

$$B = (\gamma^2/2\left[1-\sqrt{1-(2\,k_D/\lambda_{ee}\gamma^2)^2}\right])^{1/2} \tag{10}$$

$$C_{ei} = \left(k_i^2\lambda_{ee}^2 - k_D^2\lambda_{ei}^2\right)/\left(1-\lambda_{ee}^2/\lambda_{ei}^2\right) \tag{11}$$

$$\gamma = (k_i^2 + 1/\lambda_{ee}^2)^{1/2} \tag{12}$$

$$\lambda_{ee} = (-b_1/4k_F^2)^{1/2} \tag{13}$$

$$k_i = (4\pi\, n_i {Z_i}^2 e^2/k_B T_i)^{1/2} \tag{14}$$

Figures 6–9 illustrate the 3D variations of A, B, C_{ei}, and γ^2 as functions of T_i and T_e for DT, $P^{11}B$, and D^3He fuels.

From the figures, it is evident that A, B, and C_{ei} decrease nonlinearly with increasing ion and electron temperatures, with D^3He exhibiting the largest values and DT and $P^{11}B$ showing similar, slightly lower magnitudes. Conversely, γ^2 increases nonlinearly with temperature, reaching its maximum for DT and minimum for $P^{11}B$. These results highlight the sensitivity of the effective interaction potential to both electron and ion temperatures, which is crucial for accurately modeling temperature relaxation and energy transfer in dense, non-isothermal fusion plasmas.

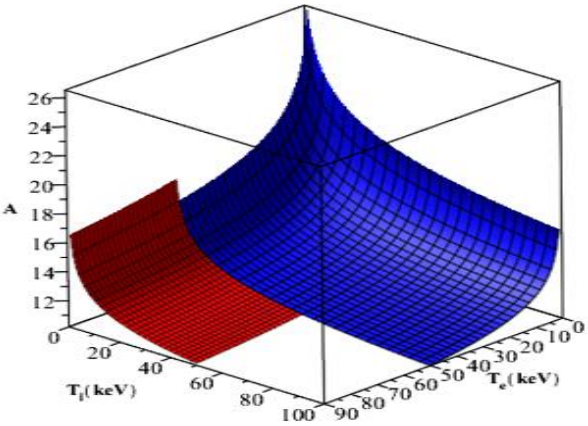

Figure 6. 3D comparison of A versus ion temperature T_i and electron temperature T_e for reactions: DT (red), D^3He (blue), and $p^{11}B$ (green) .(note: The color green is matched to the color blue because they have almost the same numerical values.)

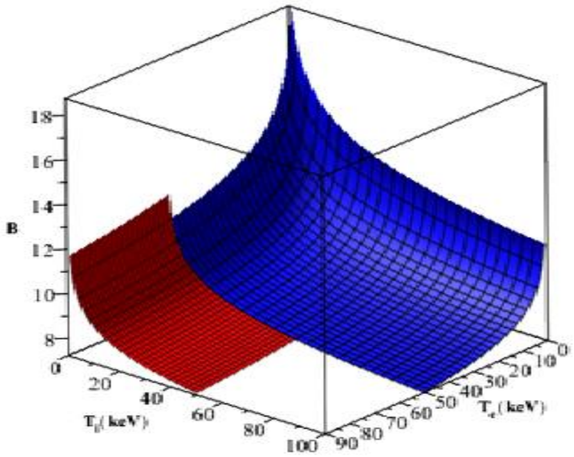

Figure 7. 3D comparison of B versus ion temperature T_i and electron temperature T_e for reactions: DT (red), D^3He (blue), and $p^{11}B$ (green) (note: The color green is matched to the color blue because they have almost the same numerical values.)

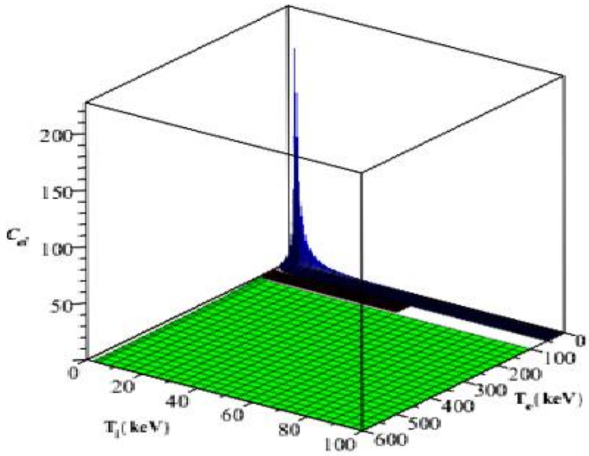

Figure 8. 3D comparison of C_{ei} versus ion temperature T_i and electron temperature T_e for reactions: DT (red), D^3He (blue), and $p^{11}B$ (green)

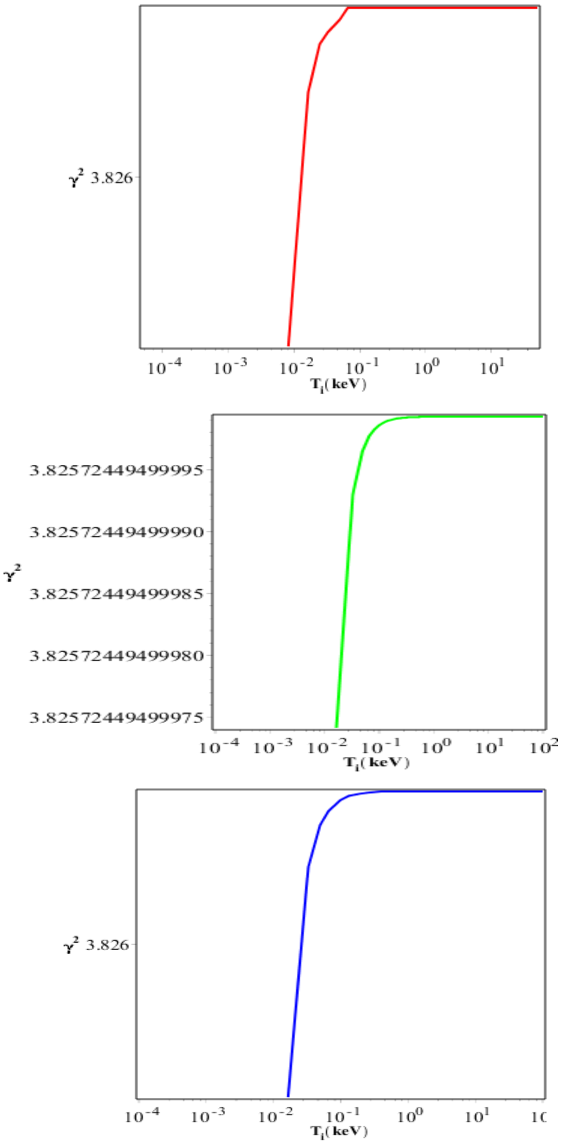

Figure 9. Temperature dependence of γ^2 for reactions: a: DT, b: $P^{11}B$, and c: D^3He

4. SP quantity

A key quantity in describing the interaction of ions with a plasma or material medium is the stopping power (SP), which quantifies the rate at which a moving particle loses its kinetic energy due to interactions with the surrounding medium [30, 36, 37]. The SP for a projectile in a plasma can be expressed as:

$$\frac{dE}{dx} = 8\pi n\left(\frac{m_{ei}}{m_i}\right)\cdot E_c\cdot \rho_\perp^2\cdot \Lambda_{ei} \tag{15}$$

Here, $E_c = \frac{m_{ei}v^2}{2}$ represents the COM (center-of-mass) kinetic energy of the interacting particles. The quantity $\rho_\perp$ is the impact parameter, defined as:$\rho_\perp = Ze^2 {E_c}^{-1}/2$. The term $\Lambda_{ei}$is the Coulomb logarithm, which accounts for the range of scattering angles contributing to energy loss and is given by:

$$w\Lambda_{ei} = \frac{1}{\rho_{\perp}^{2}} \int_{0}^{\infty} \sin^{2}\left[\frac{\chi(\rho)}{2}\right] \rho d\rho \qquad (16)$$

where $\chi(\rho)$denotes the scattering angle as a function of the impact parameter ρ. The Coulomb logarithm captures the cumulative effect of small-angle Coulomb collisions, which dominate the energy transfer in a plasma environment.

The stopping power is a critical input for modeling temperature relaxation, energy deposition, and thermalization in dense, non-isothermal plasmas. Its accurate calculation allows for precise determination of how ions transfer energy to electrons and other ions, which directly influences ignition conditions and fusion yield in systems such as DT, D^3He, and $P^{11}B$ plasmas.

5. Transport characteristics

The transport properties of plasma play a crucial role in ICF and dense plasma physics. Accurate determination of transport coefficients, including the diffusion coefficient of plasma, D, and the thermal conductivity k, is essential for modeling energy transport, particle diffusion, and thermalization in fusion fuels [38, 39]. The plasma diffusion coefficient and thermal conductivity can be expressed as:

$$D = \frac{k_B T}{m_e \nu_{eff}} \qquad (17)$$

$$k = \frac{5 n_e {k_B}^2 T}{m_e \nu_{eff}} \qquad (18)$$

where k_B is the Boltzmann constant, T is the plasma temperature, m_e is the electron mass, $n_e$is the electron density, and ν_{eff} is the effective collision frequency.

Figures 10 and 11 illustrate the variations of D and k as a function of temperature for three fusion fuels: DT, $P^{11}B$, and D^3He. As seen from the figures, both transport coefficients increase nonlinearly with temperature.

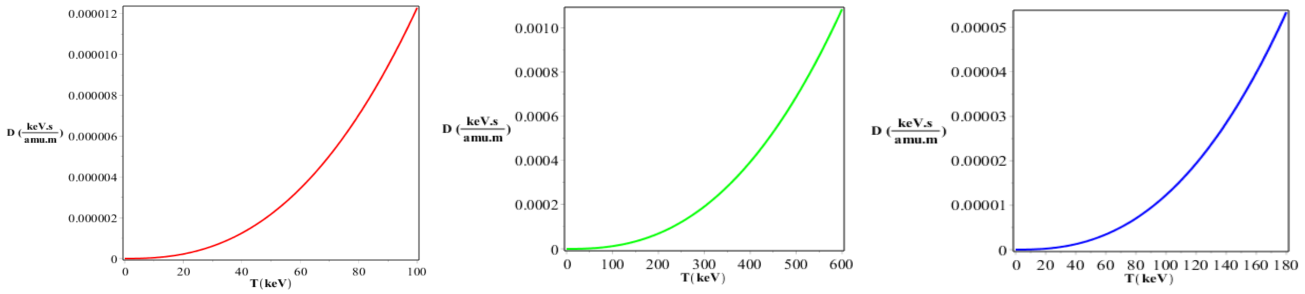

(a) (b) (c)

Figure 10. Temperature dependence of D for reactions: a: DT, b: $P^{11}B$, and c: D^3He

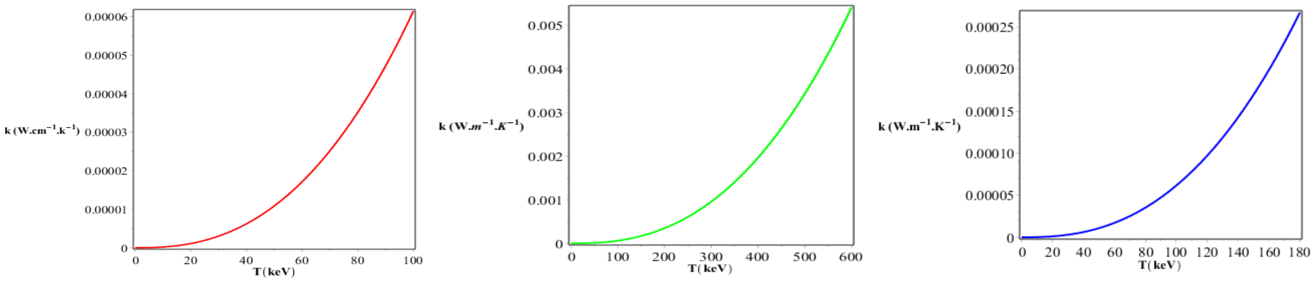

(a) (b) (c)

Figure 11. Temperature dependence of k for reactions: a: DT, b: $P^{11}B$, and c: D^3He.

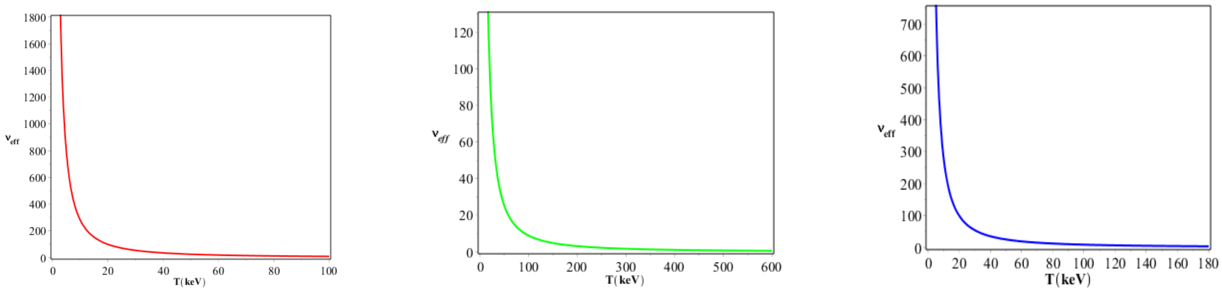

(a) (b) (c)

Figure 12. Temperature dependence of ν_{eff} for reactions: a: DT, b: $P^{11}B$, and c: D^3He

10.57647/jtap.2026.2001.07

Among the fuels studied, $P^{11}B$ exhibits the highest values of D and k, while DT shows the lowest. This reflects the combined effects of particle mass, charge, and plasma density on collisional transport.

The effective collision frequency is related to the Coulomb logarithm and the plasma parameters via [40]:

$$\nu_{eff} = (4/3)\sqrt{2\pi}e^4\Lambda_{ei}/\sqrt{m_e}(k_B T)^{3/2} \qquad (19)$$

Figure 12 shows the variations of ν_{eff} as a function of plasma temperature for DT, $P^{11}B$, D^3He and fuels. It is observed that ν_{eff} decreases nonlinearly with increasing temperature, with the highest value corresponding to DT and the lowest to $P^{11}B$.

These transport properties are critical for evaluating temperature relaxation, energy deposition, and particle transport in dense non-isothermal plasmas. Understanding these coefficients allows for accurate predictions of plasma behavior under conditions relevant to ICF experiments and aneutronic fusion systems.

6. TR quantity

TR (temperature relaxation) in dense plasmas is a fundamental process governing energy transfer between electrons and ions, particularly in fusion-relevant conditions. In non-isothermal plasmas, the relaxation rate depends on density, temperature, and inter-particle interactions, and can be accurately described using effective interaction potentials and the Coulomb logarithm [40 , 41]. The electron-ion TR rate is expressed as:

$$\frac{dT_e}{dt} = -\frac{T_e - T_i}{\tau_{ei}} \cdot \frac{dT_i}{dt} = -\frac{T_i - T_e}{\tau_{ei}} \qquad (20)$$

where τ_{ei} is the characteristic electron-ion equilibration time:

$$\tau_{ei} = \frac{3m_e m_i}{8\sqrt{2\pi}ne^2\Lambda_{ei}}\left(\frac{k_B T_e}{m_e} + \frac{k_B T_i}{m_i}\right)^{3/2} \qquad (21)$$

Figure 13 compares the 3D variation of τ_{ei} as a function of T_e and T_i for DT, $P^{11}B$, and D^3He plasmas. It is observed that τ_{ei} increases more significantly with increasing T_e than T_i, following the order $\tau_{ei,p11B} > \tau_{ei,DT} > \tau_{ei,D3He}$.

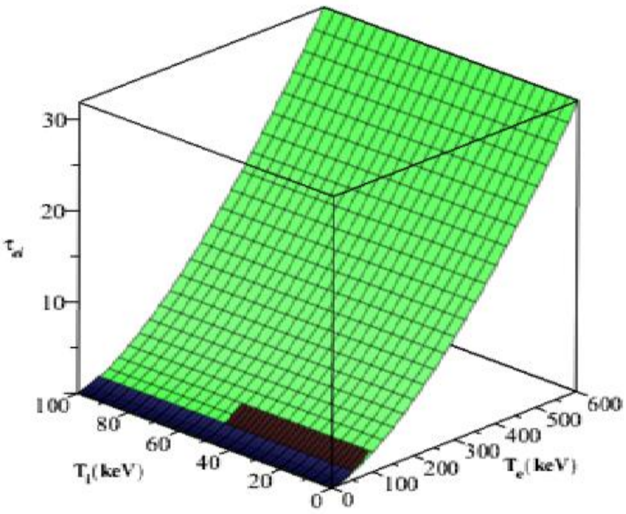

Figure 13. 3D Comparison of the three-dimensional diagram of variationsτ_{ei} versus ion temperature T_i and electron temperature T_e for reactions: DT (red), D^3He (blue), and $p^{11}B$ (green)

The plasma equation of state (EOS), including interaction contributions, can be written as:

$$P = \frac{2\pi}{3}\sum_{\alpha.\beta} \frac{n_\alpha n_\beta e_\alpha^2 e_\beta^2}{k_B T_{\alpha\beta}\gamma^2\sqrt{1-(2k_D/\lambda_{ee}\gamma^2)^2}} \times \left[\frac{1/\lambda_{ee}{}^2 - B^2}{B(1 - B^2\lambda_{\alpha\beta}{}^2)} - \frac{1/\lambda_{ee}{}^2 - A^2}{A(1 + A^2\lambda_{\alpha\beta}{}^2)}\right] + P_\lambda + P_{ideal} \qquad (22)$$

where P_{ideal} is the ideal gas pressure, and P_λ accounts for quantum and correlation effects:

$$P_\lambda = 2\pi e^2\{2Z_i n_i n_e \lambda_{ei}{}^2 - n_e{}^2\lambda_{ee}{}^2 + Z_i n_i n_e \lambda_{ei} e^2/[12k_B T_{ei}(1 + C_{ei})]\} \qquad (23)$$

Figures 14 and 15 illustrate the behavior of P_{ideal} and P for the three fusion fuels. Both pressures increase with temperature, but the nonlinear interplay between T_i and T_e in dense plasmas leads to differences among fuels. Specifically, plasma pressure satisfies $P_{D3He} > P_{DT} > P_{p11B}$.

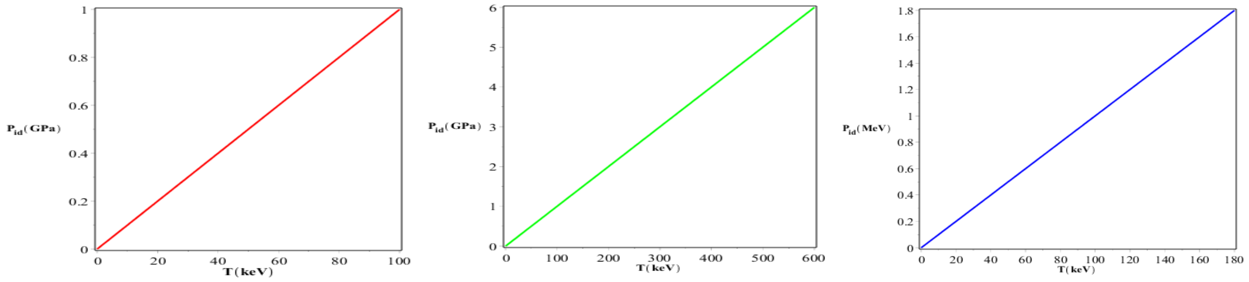

(a) (b) (c)

Figure 14. Temperature dependence of P_{ideal} for reactions: a: DT, b: $P^{11}B$, and c: D^3He

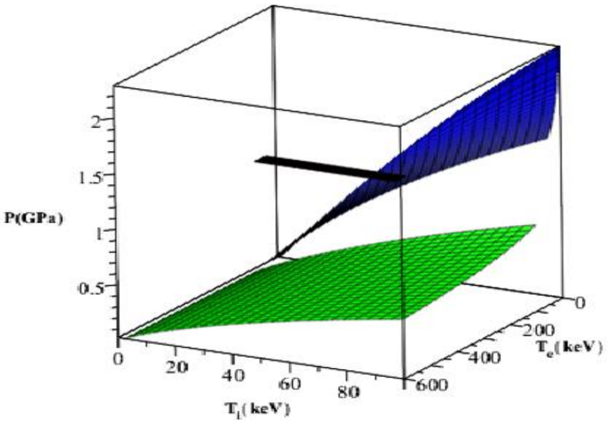

Figure 15. 3D Comparison of the three-dimensional variations of P (plasma pressure) versus ion temperature T_i and electron temperature T_e for reactions: DT (red), D^3He (blue), and $p^{11}B$ (green)

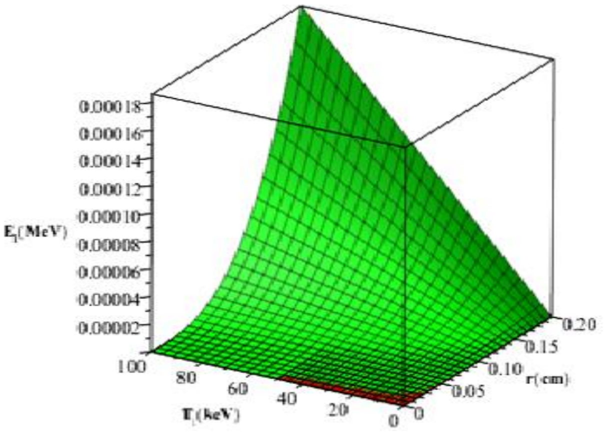

Figure 16. 3D Comparison E_i (total internal energy of ions in hot spot) versus temperature T and r for reactions: DT (red), D^3He (blue), and $p^{11}B$ (green)

To describe energy dynamics in hot spots, we introduce the three-temperature model (electron Te, ion Ti, and radiation Tr) [42].

The internal energy of ions within a hot spot is:

$$E_i = VC_{Vi}K_B T_i \rho_0 \tag{24}$$

where C_{Vi} is the ion specific heat at constant volume, V is the hot spot volume, and ρ_0 is the initial density.

The rate of energy change is:

$$\frac{dE_i}{dt} = V_{\tilde{q}_i}(T_i\,; r; T_e\,) \tag{25}$$

with $\tilde{q}_i$ representing the net energy generation rate per unit volume. The classical expressions for specific heats are $C_{Vi} = \frac{3}{2}\frac{k_B}{\bar{m}_i}$ for ions and $C_{Ve} = \frac{3}{2}\frac{\bar{Z}k_B}{\bar{m}_i}$ for electrons. The special relation energy in a constant volume is: $C_{Vr} = \frac{1}{\rho_0}\frac{16\sigma_B}{c}T_r^3$. The radiation energy density is given by: $E_r = 4T_r^4\,\sigma_B/c\rho_0$. Figures 17 and 18 show the nonlinear increase of E_r and C_{Vr} with radiation temperature T_r , highlighting the dominant role of radiation at high temperatures due to the T_r^4 dependence of energy density.

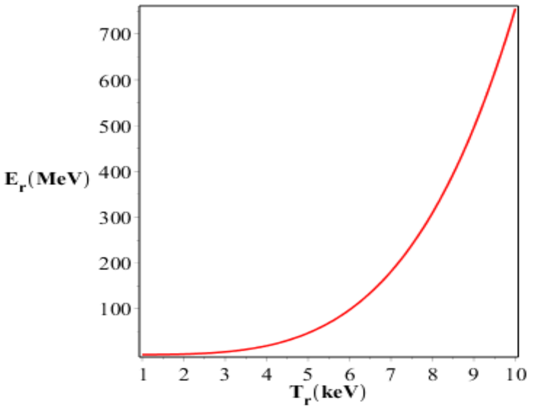

Figure 17. Variations of E_r (special relation energy) as a function of T_r(keV)

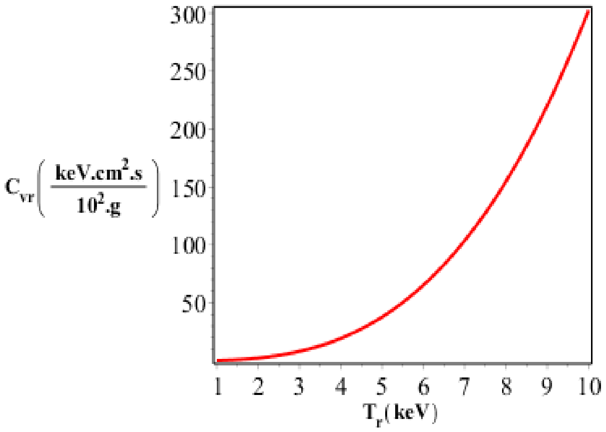

Figure 18. variations of C_{Vr} (special relation heat) as a function of T_r(keV)

7. Net energy

The net energy (NE) release rate for ions in a fusion plasma is a key parameter for evaluating the performance of thermonuclear hot spots. It can be expressed as:

$$q_i(T_e\,; T_i; x) = -A_{ie}(T_i - T_e) + S_i \tag{26}$$

Here, S_i represents the deposited energy, primarily due to the stopping of alpha particles. Because the characteristic range of alpha particles is much smaller than the size of the hot spot, it is assumed that all the alpha particle energy is deposited locally. The term $A_{ie}(T_i - T_e)$accounts for energy losses from ions to electrons via Coulomb collisions, where $A_{ei} = C_{Ve} \times \nu_{eq}$ is the coefficient of energy transfer, C_{Ve} is the specific electron heat at constant volume, and $\nu_{eq}$is the electron-ion collision frequency. If Te=Ti , collisional energy exchange vanishes. The effective collision frequency is given by:

$$\nu_{eq} = \frac{8\sqrt{2\pi}}{3}\sqrt{m_e}e^4N_A^2\frac{\bar{Z}^2}{\bar{A}^2}\ln(\Lambda_{ei})\frac{\rho_0}{(k_BT_e)^{3/2}} \times\left(1 - \frac{3}{2}\frac{K_BT_i}{K_BT_e}\frac{m_e}{\bar{m}_i}\right) \tag{27}$$

Here, m_e denotes the electron mass, e is the elementary charge, N_A is Avogadro’s number, $\bar{Z}$ and $\bar{A}$ are the mean atomic number and mass number of the ion species, and ρ_0 is the plasma density. Figures 19 and 20 present the 3D variations of A_{ie} and ν_{eq} as functions of Ti and Te for the DT, D^3He, and $P^{11}B$ fuels. The key observations are: a) A_{ie} decreases with increasing Ti and Te for all three fuels, with DT exhibiting the highest values and $P^{11}B$ the lowest (Figure 19). b) ν_{eq} also decreases with increasing temperatures, with D^3He showing the highest values and $P^{11}B$ the lowest (Figure 20).

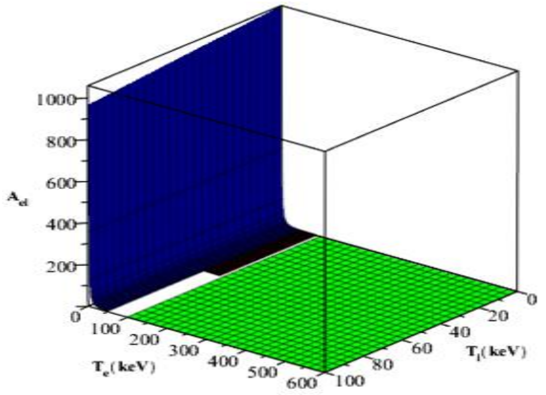

Figure 19. 3D comparison of the electron–ion energy transfer coefficient, Aei, versus ion temperature T_i and electron temperature T_e for reactions: DT (red), D^3He (blue), and $p^{11}B$ (green)

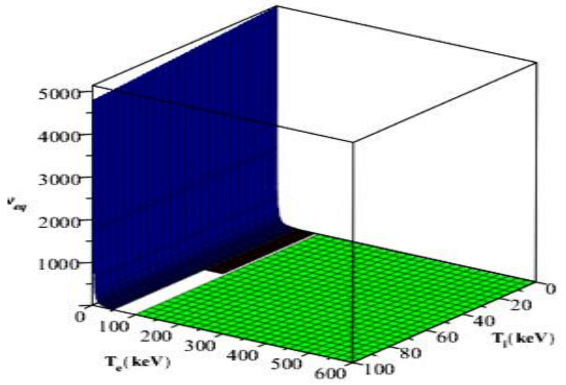

Figure 20. 3D comparison of the electron–ion energy transfer coefficient, ν_{eq}, versus ion temperature T_i and electron temperature T_e for reactions: DT (red), D^3He (blue), and $p^{11}B$ (green)

$\ln(\Lambda_{ei})$, which is used in the calculation of ν_{eq}, can be evaluated as [28]:

$$\ln(\Lambda_{ei}) = \max\left[1.\frac{1}{2e^3}\left(\frac{\bar{A}k_B^3}{\bar{Z}\pi N_A\rho_0}\right)^{1/2} T_e^{3/2} \times \left[\bar{Z} + (2\alpha_F)^{-1}\left(\frac{3k_BT_e}{m_ec^2}\right)^{1/2}\right]^{-1}\right] \tag{28}$$

Here, α_F denotes the fine-structure constant and c is the speed of light. The logarithmic term ensures an appropriate cutoff for long-range Coulomb interactions in dense plasma environments.

This formulation of the net electron energy release offers a quantitative framework for evaluating ion heating, energy deposition, and collisional losses key factors in the design and optimization of inertial confinement fusion experiments, encompassing both neutron-producing fuels (DT) and aneutronic fuels (D^3He, $p^{11}B$).

This formulation of net energy release provides a quantitative framework for analyzing ion heating, energy deposition, and collisional losses, which are critical for the design and optimization of inertial confinement fusion experiments, particularly for both neutron-producing (DT) and aneutronic fuels (D^3He, $P^{11}B$).

8. Electron energy dynamics

In fusion plasmas, the electron temperature is governed not only by direct energy deposition from charged particles but also by energy exchanges between electrons and ions, as well as between electrons and the radiation field. Consequently, the net electron energy release rate, q_e, can be expressed as:

$$q_e(T_r; T_i; T_e; x) = S_e - A_{ie}(T_e - T_i) - (A_{er} + A_c)(T_e - T_r) \tag{29}$$

Here, S_e denotes the direct energy deposition to electrons from fusion reactions, A_{ie} is the electron–ion energy transfer coefficient, A_{er} represents the electron–radiation energy transfer coefficient, and A_c accounts for energy transfer mediated by scattering processes. The coefficient A_{er} is determined by:

$$A_{er} = 2\left[\frac{2^5}{3}\frac{N_{ion}^2\bar{Z}^3e^6\rho_0}{hm_ec^3}\right]\left(\frac{2\pi k_B}{m_eK_BT_e}\right)^{1/2} \tag{30}$$

Here, N_{ion} denotes the ion number density, $\bar{Z}$ is the average ion charge, ρ_0 represents the plasma density, m_e is the electron mass, e is the elementary charge, c is the speed of light, and h is Planck’s constant. Figure 21 depicts the temperature dependence of A_{er} for DT, D^3He, and $P^{11}B$ fuels. It is evident that A_{er} increases with T_e for all fuel types, with $P^{11}B$ showing the highest values and DT the lowest. This behavior results from the inverse proportionality of A_{er} to $T_e^{1/2}$.

The scattering-mediated energy transfer coefficient, A_c, can be expressed as:

$$A_c = \frac{128}{3}\frac{\pi}{m_ec^2}\sigma_BN_er_c^2K_BT_r^4 \tag{31}$$

Here, N_e denotes the electron number density, r_c is the classical electron radius, σ_B is the Stefan–Boltzmann constant, and T_r represents the radiation temperature.

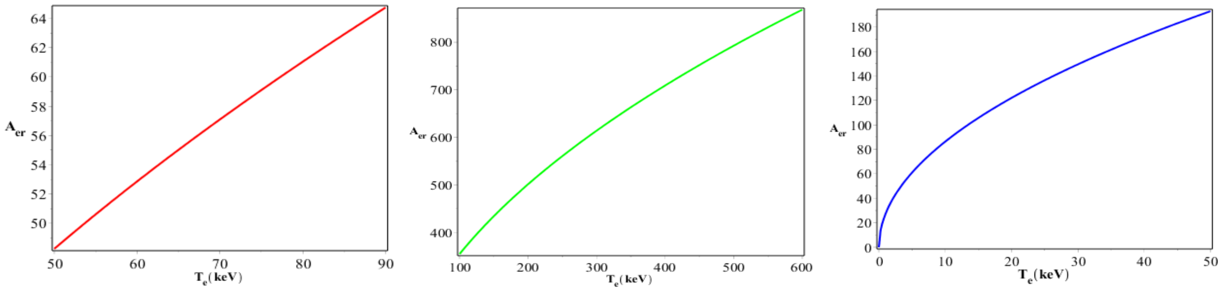

(a) (b) (c)

Figure 21. Temperature dependence of A_{er} (the energy transfer coefficient between electron and radiation) as a function of T_e(keV) for reactions: a: DT, b: $P^{11}B$, and c: D^3He

Figure 22 illustrates the variation of Ac with T_r, revealing a pronounced nonlinear increase attributed to its T_r^4 dependence. The coefficients A_{ie}, A_{er}, and A_c carry units of MJ/(cm^3·keV·s),, which guarantees dimensional consistency in the treatment of energy exchange processes. These parameters play a central role in accurately describing electron energy evolution, thermal transport, and the broader thermodynamic behavior of the plasma in both neutron-producing (DT) and aneutronic (D^3He and $P^{11}B$) fusion systems.

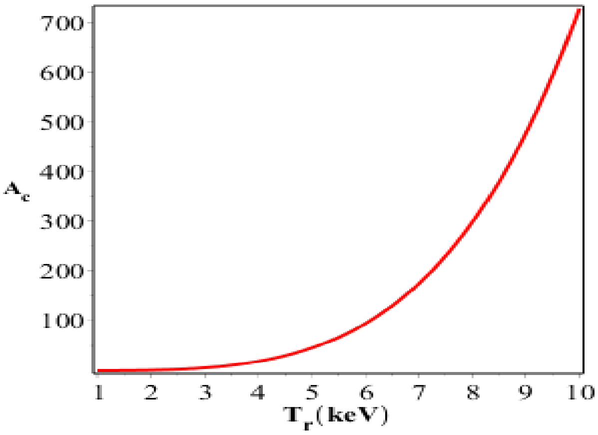

Figure 22. Variations of A_c (energy transfer coefficient) versus T_r(keV)

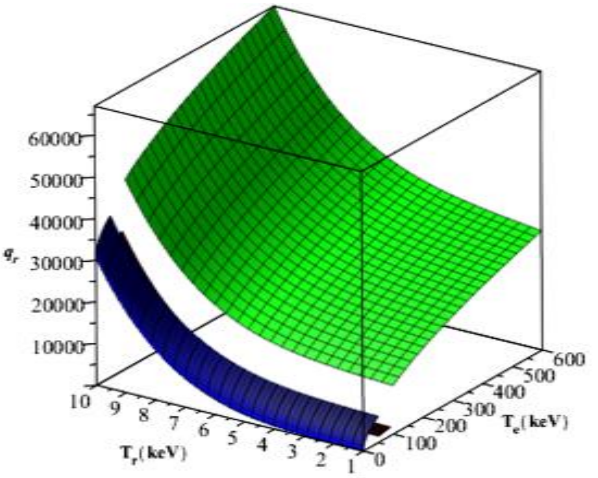

Figure 23. 3D comparison of the variation in q_r (net radiative energy gain) versus the radiation temperature T_r and electron temperature T_e for the three fusion fuel cycles DT (red), D^3He (blue), and $P^{11}B$ (green)

9. Radiation energy dynamics

The radiative component of the plasma energy, q_r, characterizes the net exchange of energy between the electrons and the radiation field, as well as the energy emitted through radiative processes. It is formulated as:

$$q_r(T_e\,;T_r;x) = -\frac{3\sigma_B K_B T_r^4}{\rho_0 x} \qquad (32)$$

$$+(A_{er}-A_c)(K_B T_e - K_B T_r)$$

In this expression, T_e and T_r denote the electron and radiation temperatures, respectively; σ_B is the Stefan–Boltzmann constant; ρ_0 is the plasma density; and x represents the characteristic length scale of the plasma. The second term, $(A_{er}-A_c)(K_B T_e - K_B T_r)$, quantifies the bidirectional energy transfer between the electron population and the radiation field, whereas the second term accounts for radiative energy losses from the plasma volume. Figure 23 presents the 3D dependence of $q_r$on T_r and T_e for DT, D^3He, and $P^{11}B$ fuels. The results demonstrate that $q_r$rises monotonically with increasing T_r and T_e for all three fuel types. Among them, $P^{11}B$ yields the largest radiative energy gain, whereas DT produces the smallest, reflecting intrinsic differences in electron–radiation coupling strength and radiative loss mechanisms across these fusion systems. This examination of radiative energy dynamics provides critical insight into energy transport and loss mechanisms in non-isothermal plasmas, particularly within high-density ICF targets and aneutronic fuel configurations. Precise characterization of q_r is vital for refining ignition criteria and enhancing the overall energy yield in thermonuclear plasma systems.

10. Results and discussion

The analysis of the plasma parameters for DT, D^3He, and $P^{11}B$ fuels reveals consistent trends in the behavior of electron-ion interaction time (τ_{ei}) and plasma pressure (P) as functions of ion (Ti) and electron (Te) temperatures. Figure observations indicate that τ_{ei} decreases with increasing electron temperature, while P increases with electron temperature at fixed ion temperatures. The maximum τ_{ei} occurs for $P^{11}B$, followed by DT and D^3He, whereas the highest plasma pressure is observed for $P^{11}B$, then D^3He, and finally DT. Similarly, other key parameters including the electron screening parameter (Z), plasma degeneracy (θ\), effective interaction potential (γ^2), ideal gas pressure (P_{ideal}), plasma diffusion coefficient (D), and thermal conductivity (k) show characteristic behaviors as functions of temperature (T). Initially constant at low temperatures, these parameters increase nonlinearly with temperature. The highest values of Z, θ, k, P_{ideal}, and D are observed for $P^{11}B$, followed by D^3He and DT, whereas γ^2\ reaches its maximum in DT, followed by D^3He and $P^{11}B$.

Further investigation of plasma properties, including the electron effective velocity (u), effective collision frequency (ν_{eff}), ion polarization function ($\Pi_{ion}(k)$), thermal wavelength (λ_{ei}), and the parameters A, B, and C_{ei}, reveals a similar trend with both Ti and Te.

These quantities typically decrease initially, remain approximately constant, and then reach a maximum at higher temperatures. The highest values of u are observed for D^3He, followed by $P^{11}B$ and DT. Parameters ν_{eff}, A, B, λ_{ei}, and C_{ei} follow the trend D^3He > DT > $P^{11}B$, while $\Pi_{ion}(k)$ is maximal for DT, then D^3He, and minimal for $P^{11}B$.

The summary of these behaviors is provided in Table 1, which highlights the relative magnitude and temperature dependence of all examined plasma parameters. Notably:

- Electron-ion interaction time (τ_{ei}) is highest for $P^{11}B$, reflecting its slower thermal equilibration.
- Plasma diffusion and thermal conductivity (D and k) are also largest in $P^{11}B$, indicating enhanced energy transport.
- Plasma pressure (P) and ideal gas contribution (P_{ideal}) are maximized for $P^{11}B$ due to stronger electron-ion coupling and reduced radiative losses.
- Electron-radiation energy transfer (A_{er}) and radiative energy gain (q_r) are substantially higher for $P^{11}B$, consistent with its aneutronic nature and lower neutron production.

These results emphasize the importance of fuel selection and temperature optimization in inertial confinement fusion, particularly when aiming to maximize net energy gain and control radiative losses.

The trends in Table 1 provide a comprehensive benchmark for comparing DT, D^3He, and $P^{11}B$ fuels under dense plasma conditions.

Table 1. Overview of the outcomes obtained from our calculations across different parameters

Quantity	range DT	range D^3He	range $P^{11}B$	Results
u	$100000 < u < 0$	$25000 < u < 0$	$1200 < u < 0$	$D^3He > P^{11}B > DT$
$\mathcal{Z}$	$0 \le Z \le 0.00009$	$0 \le Z \le 0.0004$	$0 \le Z \le 0.008$	$P^{11}B > D^3He > DT$
θ	$0 \le \theta \le 0.10$	$0 \le \theta \le 0.18$	$0 \le \theta \le 0.6$	$P^{11}B > D^3He > DT$
Π_{ion}	$0 \le \Pi_{ion} \le 1.2$	$0 \le \Pi_{ion} \le 0.6$	$0 \le \Pi_{ion} \le 0.6$	$DT > D^3He, P^{11}B$
λ_{ei}	$2200 < \lambda_{ei} < 0$	$5000 < \lambda_{ei} < 0$	$1800 < \lambda_{ei} < 0$	$DT > D^3He > P^{11}B$
A	$17 < A < 0$	$28 < A < 0$	$16 < A < 0$	$D^3He > DT > P^{11}B$
B	$12 < B < 0$	$20 < B < 0$	$11 < B < 0$	$D^3He > DT > P^{11}B$
γ^2	$3.826 < \gamma^2 < 0$	$3.826 < \gamma^2 < 0$	$3.825 < \gamma^2 < 0$	$DT, D^3He > P^{11}B$
C_{ei}	$3 < C_{ei} < 0$	$700 < C_{ei} < 0$	$14 < C_{ei} < 0$	$D^3He > DT > P^{11}B$
D	$0.000012 < D < 0$	$0.00005 < D < 0$	$0.00100 < D < 0$	$P^{11}B > D^3He > DT$
k	$0 \le k \le 0.000006$	$0 \le k \le 0.00025$	$0 \le k \le 0.005$	$P^{11}B > D^3He > DT$
ν_{eff}	$1800 < \nu_{eff} < 0$	$700 < \nu_{eff} < 0$	$120 < \nu_{eff} < 0$	$D^3He > DT > P^{11}B$
τ_{ei}	$2.4 < \tau_{ei} < 0$	$1 < \tau_{ei} < 0$	$30 < \tau_{ei} < 0$	$P^{11}B > DT > D^3He$
P_{ideal}	$1 < P_{ideal} < 0$	$1.8 < P_{ideal} < 0$	$6 < P_{ideal} < 0$	$P^{11}B > D^3He > DT$
P	$0.99999999995 < P\ 0$	$0.99999999998 < P < 0$	$0.99999999999 < P < 0$	$P^{11}B > D^3He > DT$
E_i	$0 \le E_i \le 0.00007$	$0 \le E_i \le 0.00014$	$0 \le E_i \le 0.00018$	$D^3He > P^{11}B > DT$
E_r	$700 < E_r < 0$	$700 < E_r < 0$	$700 < E_r < 0$	Independent on selected fuel
C_{Vr}	$300 < C_{Vr} < 0$	$300 < C_{Vr} < 0$	$300 < C_{Vr} < 0$	Independent on selected fuel
A_{ei}	$0.10 < A_{ei} < 0$	$0.5 < A_{ei} < 0$	$0.18 < A_{ei} < 0$	$D^3He > P^{11}B > DT$
ν_{eq}	$2.4 < \nu_{eq} < 0$	$0.5 < \nu_{eq} < 0$	$1 < \nu_{eq} < 0$	$D^3He > DT > P^{11}B$
A_{er}	$64 < A_{er} < 0$	$180 < A_{er} < 0$	$800 < A_{er} < 0$	$P^{11}B > DT > D^3He$
A_c	$700 < A_c < 0$	$700 < A_c < 0$	$700 < A_c < 0$	Independent on selected fuel
q_r	$30000 < q_r < 0$	$35000 < q_r < 0$	$60000 < q_r < 0$	$P^{11}B > D^3He > DT$

11. Conclusions

Our analysis demonstrates that the total internal energy of ions in the fuel-pellet hot spot rises consistently as the ion, electron, and radiation temperatures increase for all three fusion fuel types DT, D^3He, and $P^{11}B$. The specific radiative energy and radiative heat, together with the electron–radiation energy exchange coefficient, depend explicitly on the radiation and electron temperatures, showing a strictly monotonic growth as these temperatures rise in each fuel system. The overall energy gain is found to be highly sensitive to both electron and radiation temperatures, improving substantially with their elevation across the three fusion reactions. In contrast, the electron–ion energy transfer coefficient and the ion–electron collision frequency diminishes with increasing electron temperature, while both quantities grow as the ion temperature increases. Collectively, these behaviors underscore the decisive influence of temperature-dependent energy-exchange pathways in governing the efficiency and stability of dense, non-isothermal plasmas relevant to inertial confinement fusion and advanced aneutronic fusion concepts.

Authors Contribution

All the authors have participated sufficiently in the intellectual content, conception and design of this work or the analysis and interpretation of the data (when applicable), as well as the writing of the manuscript.

Availability of data and materials

The data that supports the findings of this study are available upon reasonable request to corresponding author.

Conflict of interests

The authors declare no conflict of interest.

References

[1] Brezinsek, S., Dhard, C. P., & Jakubowski, M. Plasma–surface interaction in the stellarator W7-X: conclusions drawn from operation with graphite plasma-facing components. *Nucl. Fusion*, **62**, 016006 (2022).

[2] Adlparvar, S., Miraboutalebi, S., Sadat Kiai, S. M., & Rajaee, L. Overdense plasma heating in Wendelstein 7-X (W7-X) stellarator. *Fusion Eng. Des.*, **7**, 1965–1970 (2017).

[3] Wurden, G. A. et al. Magneto-inertial fusion. *J. Fusion Energ.*, **35**, 69–77 (2016)

[4] Ryzhkov, S., & Magneto, V. Inertial fusion and powerful plasma installations: A review. *Appl. Sci.*, **13**, 6658 (2023)

[5] Thio, Y. C. F. et al. Plasma-jet-driven magneto-inertial fusion. *Fusion Sci. Technol.*, **75**, 49–52 (2019)

[6] Ryzhkov, S. V., & Chirkov, A. Y. Alternative fusion fuels and systems. CRC Press, Abingdon, UK (2018)

[7] Gotchev, O. V. et al. Laser-driven magnetic-flux compression in high-energy-density plasmas. *Phys. Rev. Lett.*, **103**, 215004 (2009)

[8] Riley, D. Generation and characterization of warm dense matter with intense lasers. *Plasma Phys. Control. Fusion*, **60**, 014033 (2017)

[9] Falk, K. Experimental methods for warm dense matter research. *High Power Laser Sci. Eng.*, **6**, e20 (2018)

[10] Bonitz, M., Dornheim, T., Moldabekov, Z. A., Zhang, S., Hamann, P., Kählert, H., et al. Ab initio simulation of warm dense matter. *Phys. Plasmas*, **27**, 042710 (2020)

[11] Gourdain, P.-A. The generation of warm dense matter samples using fast magnetic compression. *IEEE Trans. Plasma Sci.*, **43**, 2547–2552 (2015)

[12] Knapp, P., Beckwith, K., Cochrane, K., Clay, R. C. III, & Mattsson, T. Experimental validation of dense plasma transport models using the Z-machine. Sandia National Lab. Tech. Rep. (2019)

[13] Sinars, D. et al. Review of pulsed power-driven high energy density physics research on Z at Sandia. *Phys. Plasmas*, **27**, 070501 (2020)

[14] Prenkel, R. T., Silvestri, L. G., Murillo, M. S., & Bergeson, S. D. Temperature relaxation in strongly-coupled binary ionic mixtures. *Nat. Commun.*, **13**, 15 (2022)

[15] Garbett, W. J., & Chapman, D. A. Ignition calculations using a reduced coupled-mode electron-ion energy exchange model. *J. Phys.: Conf. Ser.*, **688**, 012019 (2016).

[16] Faussurier, G., & Blancard, C. Temperature relaxation in dense plasma mixtures. *Phys. Rev. E*, **94**, 033210 (2016).

[17] Adrian, P. J. et al. Measurements of ion-electron energy-transfer cross section in high-energy-density plasmas. *Phys. Rev. E*, **106**, L053201 (2022).

[18] Benedict, L. X. et al. Molecular dynamics studies of electron-ion temperature equilibration in hydrogen plasmas within the coupled-mode regime. *Phys. Rev. E*, **95**, 043202 (2017).

[19] Ma, Q. et al. Extremely low electron-ion temperature relaxation rates in warm dense hydrogen: interplay between quantum electrons and coupled ions. *Phys. Rev. Lett.*, **122**, 015001 (2019).

[20] Svensson, P. et al. Development of a new quantum trajectory molecular dynamics framework. *Philos. Trans. A Math. Phys. Eng. Sci.*, **381**, 20220325 (2022).

[21] Gao, C.-Z. et al. Assessment of the electron-proton energy relaxation rates extracted from molecular dynamics simulations in weakly-coupled hydrogen plasmas. *Phys. Rev. E*, **107**, 015203 (2023).

[22] Silvestri, L. G., Sprenkle, R. T., Bergeson, S. D., & Murillo, M. S. Relaxation of strongly coupled binary ionic mixtures in the coupled mode regime. *Phys. Plasmas*, **28**, 062302 (2021).

[23] Dey, A., Chandra, S., Das, C., Mandal, S., & Das, T. Rogue wave generation through nonlinear self-interaction of electrostatic waves in dense plasma. *IEEE Trans. Plasma Sci.*, **50**, 1557–1564 (2022).

[24] Ghosh, T., Pramanick, S., Sarkar, S., Dey, A., & Chandra, S. Chaotic scenario in three-component Fermi plasma. *Afr. Rev. Phys.*, **15**, 2020.

[25] Thakur, S., Das, C., & Chandra, S. Stationary structures in a four-component dense magnetoplasma with lateral perturbations. *IEEE Trans. Plasma Sci.*, **50**, 1545–1556 (2022).

[26] Ballav, S., Das, A., Pramanick, S., & Chandra, S. Plasma shock wave in gamma-ray bursts: Nonlinear phenomena and radiative process. *IEEE Trans. Plasma Sci.*, **50**, 1488–1494 (2022).

[27] Das, A., Ghosh, P., Chandra, S., & Raj, V. Electron acoustic Peregrine breathers in a quantum plasma with 1-D temperature anisotropy. *IEEE Trans. Plasma Sci.*, **50**, 1598–1609 (2022).

[28] Rightley, S., & Baalrud, S. D. Kinetic model for electron-ion transport in warm dense matter. *Phys. Rev. E*, **103**, 063206 (2021).

[29] Daligault, J. On the quantum Landau collision operator and electron collisions in dense plasmas. *Phys. Plasmas*, **23**, 032706 (2016).

[30] Baggott, R. A., Rose, S. J., & Mangles, S. P. D. Temperature equilibration due to charge state fluctuations in dense plasmas. *Phys. Rev. Lett.*, **127**, 035002 (2021).

[31] Simoni, J., & Daligault, J. First-principles determination of electron-ion couplings in the warm dense matter regime. *Phys. Rev. Lett.*, **122**, 205001 (2019).

[32] Daligault, J., & Simoni, J. Theory of the electron-ion temperature relaxation rate spanning the hot solid metals and plasma phases. *Phys. Rev. E*, **100**, 043201 (2019).

[33] Simoni, J., & Daligault, J. Calculation of electron-ion temperature equilibration rates and friction coefficients in plasmas and liquid metals using quantum molecular dynamics. *Phys. Rev. E*, **101**, 013205 (2020).

[34] Faussurier, G., & Blancard, C. Fast temperature relaxation model in dense plasmas. *Phys. Plasmas*, **24**, 012705 (2017).

[35] Starrett, C. E. Coulomb log for conductivity of dense plasmas. *Phys. Plasmas*, **25**, 092707 (2018).

[36] Oloumi, M., Habibi, M., & Hosseinkhani, H. An analysis of the evaluations of Coulomb logarithm and electron–ion relaxation rates in deuterium plasmas across coupling regimes. *Plasma Phys. Rep.*, **47**, 1021 (2021).

[37] Hagelaar, G. J. M., Donko, Z., & Dyatko, N. Modification of the Coulomb logarithm due to electron-neutral collisions. *Phys. Rev. Lett.*, **123**, 025004 (2019).

[38] Fletcher, L. B. et al. Electron-ion temperature relaxation in warm dense hydrogen observed with picosecond resolved x-ray scattering. *Front. Phys.*, **10**, 838524 (2022).

[39] Richardson, A. S. NRL Plasma Formulary. US Naval Research Laboratory, 37 (2020).

[40] Hayes, A. C. et al. Plasma stopping-power measurements reveal transition from non-degenerate to degenerate plasmas. *Nat. Phys.*, **16**, 432 (2019).

[41] Rygg, J. R. et al. Electron-ion thermal equilibration after spherical shock collapse. *Phys. Rev. E*, **80**, 026403 (2009).

[42] Ghosh, S., Saha, S., Chakraborty, T., Sadhukhan, K., Bhanja, R., & Chandra, S. Linear and nonlinear properties of electron acoustic waves in a viscous plasma. *Afr. Rev. Phys.*, **15**, 90 (2021)